

Vacuum energy density and pressure inside a soft wall

Agam Shayit,^{1,2,*} S. A. Fulling,^{1,3,†} T. E. Settlemyre,^{1,3,‡} and Joseph Merritt^{1,3,§}

¹*Department of Physics and Astronomy, Texas A&M University, College Station, Texas 77843-4242, USA*

²*Department of Computer Science and Engineering,*

Texas A&M University, College Station, Texas 77843-3112, USA

³*Department of Mathematics, Texas A&M University, College Station, Texas 77843-3368, USA*

(Dated: July 30, 2021)

In the study of quantum vacuum energy and the Casimir effect, it is desirable to model the conductor by a potential of the form $V(z) = z^\alpha$. Unlike the standard Dirichlet wall, this model does not violate the principle of virtual work under regularization. Previously, this “soft wall” model was formalized for a massless scalar field, and the expectation value of the stress tensor was expressed in terms of the reduced Green function of the equation of motion. In the limit of interest $\alpha \gg 1$, which corresponds to the Dirichlet wall, a closed-form expression for the reduced Green function cannot be found. Here we develop a piecewise approximation scheme incorporating the perturbative and WKB expansions of the Green function, as well as an interpolating spline in the region where neither expansion is valid. We then apply the scheme to the sextic soft wall and use it to compute the renormalized energy density and pressure inside the cavity for various conformal parameters. The consistency of the results is verified by comparison to their numerical counterparts and verification of the trace anomaly and the conservation law. Finally, we use the approximation scheme to reproduce the energy density inside the quadratic wall, which was previously calculated exactly.

I. INTRODUCTION

The Casimir effect in quantum field theory refers to the attractive force between the boundaries of a cavity in vacuum. This attractive force is induced by the energy gradient resulting from the modification of the normal modes of the quantum field inside the cavity. The existence of this force entails that the expectation value of the quantum field is nonzero in vacuum. This force was first derived by Casimir in [1] for an electromagnetic field and a perfect conductor. Many later works, such as [2–4], simplify Casimir’s model by replacing the EM field and the conductor with a scalar field and Dirichlet boundary conditions.

In order to produce physical results in models in quantum field theory, one must regularize them first. This is most commonly done by imposing an ultraviolet cutoff, which avoids subtraction of infinite quantities. Since the scalar field with Dirichlet boundary conditions (“hard wall”) model was shown in [5] to violate the principle of virtual work under ultraviolet cutoffs, it is unsuitable for contemporary analysis of phenomena in Casimir physics.

A more realistic model of the boundary is a power-law potential (“soft wall”). This model is computationally feasible and does not violate the principle of virtual work under regularization. In this paper, we restrict our analysis to a single massless scalar field, ϕ , interacting with a single soft wall. Similar work on the electromagnetic field in inhomogeneous dielectric media includes [6–9].

In Sec. II, we summarize previous results [10–14] regarding the stress tensor and Green function inside a soft wall. The Appendix of [12] reviews still earlier related work by other researchers. Secs. III and IV extend the perturbation theory and WKB calculations performed in [12, 13] to arbitrary order. In Sec. V, we use these approximations to develop a piecewise approximation scheme for the Green function and its second derivative. We then compare the piecewise approximations to their numerical counterparts.

We use the analytical and numerical approximations to calculate the energy density and pressure inside the sextic soft wall. These results are plotted in Secs. VI and VII. In Sec. VIII, we verify that the approximated stress tensor upholds the trace identity and conservation law.

Finally, in Sec. IX, we use the approximation scheme developed in Sec. V to reproduce the energy density inside the quadratic wall. We then compare the results to their analytical counterparts calculated in [13].

Our conclusion, Sec. X, includes a discussion of the prospects for eliminating in future work certain *ad hoc* elements in the approximation scheme. It is followed by two appendices, the first on the numerical solution and the second on previously attempted approximation schemes.

* agam@tamu.edu

† Corresponding author.

fulling@math.tamu.edu; <http://www.math.tamu.edu/~fulling>

‡ tommy7410@tamu.edu

§ Present address: Department of Physics, University of Washington, Seattle, Washington 98195-1560, USA; jm117@uw.edu

This paper summarizes and extends [15].

II. THE SOFT WALL MODEL

To overcome the violation of the principle of virtual work under regularization, it was proposed in [10, 11] to replace the Dirichlet wall with the “softer” counterpart

$$V(z) = \begin{cases} 0 & \text{if } z \leq 0, \\ z^\alpha & \text{if } z > 0. \end{cases} \quad (2.1)$$

Here $\alpha > 0$ is a stiffness parameter, which we ordinarily take to be an integer to avoid extraneous singular behavior at the origin. This potential interacts with a massless Klein–Gordon field according to [13, Eq. (1.2)], namely

$$\mathcal{L} = -\frac{1}{2}\partial_\mu\phi\partial^\mu\phi - \frac{V}{2}\phi^2. \quad (2.2)$$

This Lagrangian density yields the generalized Klein–Gordon equation

$$-\frac{\partial^2\phi}{\partial t^2} + \nabla^2\phi = V(z)\phi, \quad (2.3)$$

where without loss of generality one chooses units where $c = 1$ and $\hbar = 1$, so that both t and z have units of inverse mass. Indeed, V takes the place of the mass squared in the usual Klein–Gordon equation. As it stands this appears inconsistent with (2.1), so, following [10], we momentarily adopt a maximally cautious notation that makes all the free parameters explicit and their dimensions transparent:

$$V(z) = \lambda_0 \left(\frac{z}{z_0}\right)^\alpha \quad \text{if } z > 0, \quad (2.4)$$

where z_0 is a length and λ_0 is the square of a mass. This parametrization, however, is obviously redundant, because of the special scaling behavior of the power function. The strength of the potential is determined by a single coupling constant, $\hat{\lambda} = \lambda_0 z_0^{-\alpha}$, or, alternatively, a single length scale,

$$\hat{z} = \left(\frac{z_0^\alpha}{\lambda_0}\right)^{\frac{1}{\alpha+2}}.$$

(Since α is assumed to be positive, the singularity at $\alpha = -2$ is no cause for concern.) Then

$$V(z) = \hat{\lambda} z^\alpha = \frac{1}{\hat{z}^2} \left(\frac{z}{\hat{z}}\right)^\alpha. \quad (2.5)$$

However, we still have one degree of freedom left in the fundamental units: We can choose the unit of length (or mass) so that $\hat{z} = 1$ (or $\hat{\lambda} = 1$). Then all explicit constants disappear from the formula for V . With this convention, $V(1) = 1$ for all α and the potential forms an increasingly steep wall near $z = 1$ as $\alpha \rightarrow \infty$.

The reduced Green function of the field equation inside a soft wall, evaluated at coincident points, was derived in [11] as

$$g_\kappa(z) = \frac{1}{W} \left(F_\kappa(z)G_\kappa(z) - F_\kappa(z)^2 \frac{G_\kappa(0) - G'_\kappa(0)/\kappa}{F_\kappa(0) - F'_\kappa(0)/\kappa} \right). \quad (2.6)$$

Here $\kappa > 0$ is the imaginary wave number, z is the displacement along the axis perpendicular to the soft wall, and $W = W(F_\kappa, G_\kappa)$ is the Wronskian of $F_\kappa(z)$ and $G_\kappa(z)$, which are solutions of the differential equation

$$\left(-\frac{\partial^2}{\partial z^2} + V(z) + \kappa^2 \right) y = 0, \quad (2.7)$$

such that $F_\kappa(z)$ decays at positive infinity and $G_\kappa(z)$ is linearly independent of $F_\kappa(z)$.

By normalizing the boundary conditions of $F_\kappa(z)$ and $G_\kappa(z)$ to be

$$G_\kappa(0) = 0, \quad G'_\kappa(0) = 1, \quad F_\kappa(0) = 1, \quad (2.8)$$

Eq. (2.6) was simplified to

$$\begin{aligned} g_\kappa(z) &= F_\kappa(z)G_\kappa(z) + \gamma(\kappa)F_\kappa(z)^2, \\ \gamma(\kappa) &= \frac{1}{\kappa - F'_\kappa(0)}. \end{aligned} \quad (2.9)$$

As shown in [13, Sec. II], the vacuum expectation value $\langle \phi^2 \rangle$ is given by the formula $I[g_\kappa(z)]$, where

$$I[h(\kappa)] \equiv \frac{1}{2\pi^2} \int_0^\infty d\kappa \kappa^2 h(\kappa) \frac{\sin \kappa \delta}{\kappa \delta} \quad (2.10)$$

and δ is a point-separation parameter, [13, Eq. (2.8)], which henceforth will be taken to zero in all equations where the regularization is no longer necessary. Expressions for the components of the corresponding renormalized stress tensor inside a soft wall [13, Eq. (5.11)] were also derived. The interpretation of the renormalization is discussed in [14]. These expressions involve terms of the form

$$I \left[\kappa^a f(z) \frac{\partial^b (g_\kappa(z) - \tilde{g}_\kappa(z))}{\partial z^b} \right], \quad (2.11)$$

where $a, b \in \{0, 2\}$ and the function $f(z)$ is either a constant or the soft wall (2.1). The second-order WKB approximation of the Green function, $\tilde{g}_\kappa(z)$, is given in [13, Eq. (3.1)] as

$$\tilde{g}_\kappa(z) = \frac{1}{2\sqrt{\kappa^2 + V(z)}} - \frac{V''(z)}{16(\kappa^2 + V(z))^{5/2}} + \frac{5V'^2(z)}{64(\kappa^2 + V(z))^{7/2}}. \quad (2.12)$$

As will be evident in the next sections, it is instructive to break up the integral (2.11) by employing a cutoff parameter Λ and defining the functionals

$$\begin{aligned} I_\Lambda[h(\kappa)] &\equiv \frac{1}{2\pi^2} \int_0^\Lambda d\kappa \kappa^2 h(\kappa), \\ J_\Lambda[h(\kappa)] &\equiv \frac{1}{2\pi^2} \int_\Lambda^\infty d\kappa \kappa^2 h(\kappa). \end{aligned} \quad (2.13)$$

The components of the stress tensor inside the linear and quadratic walls were computed exactly [13] using Eq. (2.9). These correspond to the only values of α for which exact solutions of Eq. (2.7) can be expressed in terms of standard special functions, although some properties of the solutions for general α have been studied by Faierman [16].

In order to study the Casimir effect under the soft wall model, the renormalized stress tensor should be computed for $\alpha \gg 1$. From Eq. (2.1), it is clear that when α is large, the soft wall approximates the Dirichlet wall, for which the Casimir effect was originally derived.

Since the solutions of Eq. (2.7) do not have closed-form expressions for $\alpha > 2$, we must approximate $F_\kappa(z), G_\kappa(z)$ for all $\kappa \in [0, \infty)$ in order to compute terms of the form (2.11).

III. PERTURBATION THEORY

To approximate the Green function in the small κ regime, we generate the perturbative expansions of the basis solutions $F_\kappa(z)$ and $G_\kappa(z)$ of Eq. (2.7). The coefficients of these power series are obtained from perturbation theory, as outlined in [12, Sec. III]. There, the coefficients $F_0(z), F_1(z), G_0(z)$, and $G_1(z)$, in the sense of Eq. (3.2), were computed to form first-order approximations.

For the perturbative approximations to be usable as a part of a sufficiently accurate piecewise approximation, they must be carried to a rather high order. This is done by calculating the coefficients [12, Eq. (3.12)] using the generalization of the recursion relation [12, Eq. (3.8)]

$$\begin{aligned} F_n(z) &= \frac{1}{W(i, k)} \left(k(z) \int_0^z i(a) F_{n-1}(a) da + i(z) \int_z^\infty k(a) F_{n-1}(a) da \right), \\ G_n(z) &= \frac{1}{W(i, k)} \left(k(z) \int_0^z i(a) G_{n-1}(a) da - i(z) \int_0^z k(a) G_{n-1}(a) da \right), \end{aligned} \quad (3.1)$$

where $W(i, k)$ is the Wronskian of $i(z)$ and $k(z)$, which are defined in [12, Eq. (3.3)]. The coefficients $\{F_n(z)\}_{n=2}^{30}$ were evaluated numerically, where the upper limit of the improper integral in Eq. (3.1) was replaced by $z_\infty = 3.4$ because

Mathematica cannot evaluate the integrand for large values of a properly (despite its being numerically negligible). The coefficients $\{G_n(z)\}_{n=2}^{30}$ were evaluated by expanding the appropriate integrands in Eq. (3.1) as Maclaurin series of order 40. Thus we obtained the 30th-order perturbation approximations

$$\begin{aligned} F_{\kappa \ll 1}(z) &= \sum_{n=0}^{30} F_n(z) \kappa^{2n}, \\ G_{\kappa \ll 1}(z) &= \sum_{n=0}^{30} F_n(z) \kappa^{2n}. \end{aligned} \quad (3.2)$$

The Green function is obtained by plugging these approximations into Eq. (2.9):

$$\begin{aligned} g_{\kappa \ll 1}(z) &= F_{\kappa \ll 1}(z) G_{\kappa \ll 1}(z) + \gamma_{\kappa \ll 1}(\kappa) F_{\kappa \ll 1}(z)^2, \\ \gamma_{\kappa \ll 1}(\kappa) &= \frac{1}{\kappa - F'_{\kappa \ll 1}(0)}. \end{aligned} \quad (3.3)$$

Next, we differentiate Eq. (2.9) twice and obtain

$$\partial_z^2 g_{\kappa}(z) = G_{\kappa}(z) F_{\kappa}''(z) + 2F_{\kappa}'(z) G_{\kappa}'(z) + F_{\kappa}(z) G_{\kappa}''(z) + 2\gamma(\kappa) (F_{\kappa}(z) F_{\kappa}''(z) + F_{\kappa}'(z)^2). \quad (3.4)$$

Since $F_{\kappa}(z)$ and $G_{\kappa}(z)$ are solutions of Eq. (2.7), their second derivative is known, and we obtain

$$\begin{aligned} \frac{(\partial_z^2 g_{\kappa}(z))_{\kappa \ll 1}}{2} &= F'_{\kappa \ll 1}(z) G'_{\kappa \ll 1}(z) + \gamma_{\kappa \ll 1}(\kappa) \times (F'_{\kappa \ll 1}(z)^2 + F_{\kappa \ll 1}(z)^2 (\kappa^2 + V(z))) \\ &\quad + F_{\kappa \ll 1}(z) G_{\kappa \ll 1}(z) (\kappa^2 + V(z)), \end{aligned} \quad (3.5)$$

in terms of $F_{\kappa \ll 1}(z)$, $G_{\kappa \ll 1}(z)$, and their first derivatives. We find this approach to yield a more stable perturbation series than direct differentiation of the approximation (3.3).

IV. THE WKB APPROXIMATION

For large values of either κ or z , the sought-after solutions are well-approximated by asymptotic expansions. The WKB approximations of simple decaying and growing solutions of Eq. (2.7), as well as the dominant part of the Green function (2.6), were recorded [13, Eqs. (A3) and (A5)] as

$$\begin{aligned} y(z) &\sim \frac{e^{\pm \int^z dt [q_0(t) + q_2(t) + q_4(t) + \dots]}}{\sqrt{q_0(z) + q_2(z) + q_4(z) + \dots}}, \\ \frac{F_{\kappa}(z) G_{\kappa}(z)}{W} &\sim \frac{1}{2} \frac{1}{q_0(z) + q_2(z) + q_4(z) + \dots}. \end{aligned} \quad (4.1)$$

We require that our basis solutions have the asymptotic approximations

$$\begin{aligned} \widehat{F}_{\kappa \gg 1}(z) &\equiv \frac{e^{-\int^z dt [q_0(t) + q_2(t) + q_4(t) + \dots]}}{\sqrt{q_0(z) + q_2(z) + q_4(z) + \dots}}, \\ \widehat{G}_{\kappa \gg 1}(z) &\equiv \frac{e^{+\int^z dt [q_0(t) + q_2(t) + q_4(t) + \dots]}}{2\sqrt{q_0(z) + q_2(z) + q_4(z) + \dots}}, \end{aligned} \quad (4.2)$$

with the same lower limit in both integrals. Then from Eq. (4.1) one sees that the Wronskian of the exact solutions is unity. These solutions may not have the normalization (2.8), but since Eq. (2.6) holds for any decaying and growing basis functions, plugging in $\widehat{F}_{\kappa \gg 1}(z)$ and $\widehat{G}_{\kappa \gg 1}(z)$ yields:

$$\begin{aligned} g_{\kappa \gg 1}(z) &\equiv \frac{1}{2(q_0(z) + q_2(z) + q_4(z) + \dots)} + \frac{\widehat{\gamma}(\kappa) e^{-2\int^z dt [q_0(t) + q_2(t) + q_4(t) + \dots]}}{q_0(z) + q_2(z) + q_4(z) + \dots} \sim g_{\kappa}(z), \\ \widehat{\gamma}(\kappa) &= -\frac{\widehat{G}_{\kappa \gg 1}(0) - \widehat{G}'_{\kappa \gg 1}(0)/\kappa}{\widehat{F}_{\kappa \gg 1}(0) - \widehat{F}'_{\kappa \gg 1}(0)/\kappa}. \end{aligned} \quad (4.3)$$

As shown in [17], the local functionals q_n may be obtained from a recurrence relation. (In practice, we used a slightly different form of the recursion, found in [18].) The recurrence relation can be solved in a bottom-up manner using dynamic programming. With this method, the local functionals q_1, \dots, q_n can be computed in $O(n^2)$ time.

The first five terms were kept in the prefactor and the exponential, yielding a ninth-order Fröman approximation [13, Appendix A]. The term $\widehat{\gamma}(\kappa)$ was then computed by plugging in the ninth-order Fröman approximations of $\widehat{F}_{\kappa \gg 1}(z)$ and $\widehat{G}_{\kappa \gg 1}(z)$ and taking the limit as $z \rightarrow 0$. The second derivative of the Green function is approximated as

$$(\partial_z^2 g_\kappa(z))_{\kappa \gg 1} \equiv \partial_z^2 (g_{\kappa \gg 1}(z)). \quad (4.4)$$

V. THE APPROXIMATED GREEN FUNCTION

Equipped with the approximations of the last two sections, we wish to approximate the Green function for values of κ that are too large for the perturbative expansion to be usable, but are not large enough for the WKB approximation to be valid. This process naturally contains arbitrary elements which are rooted in trial and error. These ambiguities are unavoidable and are ultimately justifiable by the results they yield (Cf. Appendix B).

The Green function and its second derivative are approximated by interpolating splines in the intermediate κ regime. For a fixed $z = z_0$, the splines are constructed to match the perturbative and WKB approximations at the boundaries of the intermediate regimes. The boundaries are defined by the endpoints κ_{L_0} , κ_{R_0} , κ_{L_2} , and κ_{R_2} for $g_\kappa(z)$ and $\partial_z^2 g_\kappa(z)$, respectively.

The general form of the splines was chosen to be a simple asymptotic expansion

$$g_{\kappa \approx 1}(z_0) = \sum_{i=1}^n \frac{A_i}{\kappa^i}, \quad (5.1)$$

$$(\partial_z^2 g_\kappa(z_0))_{\kappa \approx 1} = \sum_{i=1}^n \frac{B_i}{\kappa^i}. \quad (5.2)$$

The coefficients $\{A_i\}, \{B_i\}$ were selected to satisfy

$$\begin{aligned} \partial_\kappa^m g_{\kappa \approx 1}(z_0) \Big|_{\kappa_{L_0}} &= \partial_\kappa^m g_{\kappa \ll 1}(z_0) \Big|_{\kappa_{L_0}}, \\ \partial_\kappa^m (\partial_z^2 g_\kappa(z_0))_{\kappa \approx 1} \Big|_{\kappa_{L_2}} &= \partial_\kappa^m (\partial_z^2 g_\kappa(z_0))_{\kappa \ll 1} \Big|_{\kappa_{L_2}}, \\ \partial_\kappa^m g_{\kappa \approx 1}(z_0) \Big|_{\kappa_{R_0}} &= \partial_\kappa^m g_{\kappa \gg 1}(z_0) \Big|_{\kappa_{R_0}}, \\ \partial_\kappa^m (\partial_z^2 g_\kappa(z_0))_{\kappa \approx 1} \Big|_{\kappa_{R_2}} &= \partial_\kappa^m (\partial_z^2 g_\kappa(z_0))_{\kappa \gg 1} \Big|_{\kappa_{R_2}}, \end{aligned} \quad (5.3)$$

for all $m = 0, \dots, \frac{n-2}{2}$.

The endpoints were chosen arbitrarily to be within the domain of validity of their corresponding regimes while also being in close proximity to each other. This criterion may be formulated in a well-defined manner using the remainders of the perturbation and WKB approximations. Since these are yet to be calculated, we implement the endpoint selection by qualitative analysis of the behavior of both approximations. The spline $g_{\kappa \approx 1}(z_0)$, shown in Fig. 1, was constructed using $\kappa_{L_0} = 2$ and $\kappa_{R_0} = 6$. The spline $(\partial_z^2 g_\kappa(z_0))_{\kappa \approx 1}$, shown in Fig. 2, was constructed using $\kappa_{L_2} = 2$ and $\kappa_{R_2} = 8$. Both splines were taken to be of order $n = 8$.

Using the approximations (3.3), (4.3), and (5.1), we approximate the Green function in all κ regimes as

$$\bar{g}_\kappa(z_0) \equiv \begin{cases} g_\kappa(z_0)_{\kappa \ll 1} & \kappa < \kappa_{L_0}, \\ g_\kappa(z_0)_{\kappa \approx 1} & \kappa_{L_0} \leq \kappa \leq \kappa_{R_0}, \\ g_\kappa(z_0)_{\kappa \gg 1} & \kappa > \kappa_{R_0}. \end{cases} \quad (5.4)$$

Similarly, the approximations (3.5), (4.4), and (5.2) yield the piecewise approximation

$$\partial_z^2 \bar{g}_\kappa(z_0) \equiv \begin{cases} (\partial_z^2 g_\kappa(z))_{\kappa \ll 1} & \kappa < \kappa_{L_2}, \\ (\partial_z^2 g_\kappa(z))_{\kappa \approx 1} & \kappa_{L_2} \leq \kappa \leq \kappa_{R_2}, \\ (\partial_z^2 g_\kappa(z))_{\kappa \gg 1} & \kappa > \kappa_{R_2}. \end{cases} \quad (5.5)$$

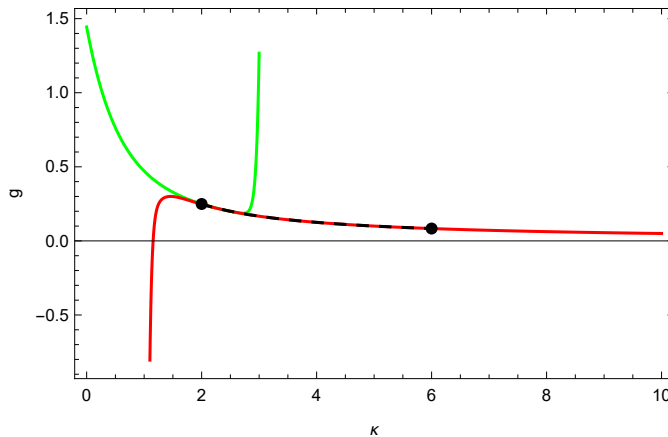


FIG. 1. The perturbative expansion (3.3) (in green), the WKB approximation (4.3) (in red), and the spline (5.1) (in black dashes) for $\alpha = 6$ and $z = 0.01$. The black dots mark $\kappa_{L_0} = 2$ and $\kappa_{R_0} = 6$. The perturbative expansion clearly diverges as κ grows, while the WKB approximation is accurate for moderate values of κ . All graphics in this paper were prepared with *Mathematica*.

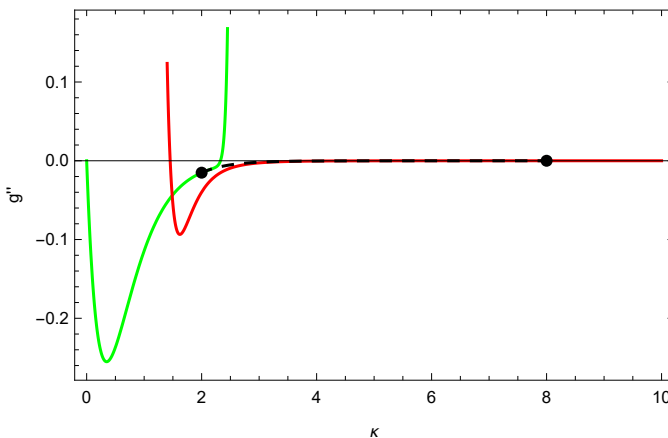


FIG. 2. The perturbative expansion (3.5) (in green), the WKB approximation (4.4) (in red), and the spline (5.2) (in black dashes) for $\alpha = 6$ and $z = 0.01$. The black dots mark $\kappa_{L_2} = 2$ and $\kappa_{R_2} = 8$.

To verify the accuracy of the piecewise approximations, we compare them to their numerical counterparts. These are obtained by solving Eq. (2.7) numerically with the boundary conditions (2.8) to obtain the numerical basis functions $\underline{F}_\kappa(z)$ and $\underline{G}_\kappa(z)$. This process is outlined in Appendix A.

The numerical Green function $\underline{g}_\kappa(z)$ and its second derivative $\underline{\partial}_z^2 \underline{g}_\kappa(z)$ are plotted in Figs. 3 and 4. They were computed from the numerical basis solutions $\underline{F}_\kappa(z)$ and $\underline{G}_\kappa(z)$ using Eq. (2.9) and the numerical equivalent of Eq. (3.5). The derivatives $\underline{F}'_\kappa(z)$ and $\underline{G}'_\kappa(z)$ were approximated by sixth-order finite difference formulae [19, 20].

The piecewise and numerical approximations presented here will be used in the next section to compute the stress tensor inside a soft wall. The terms of the form (2.11) are approximated analytically using the functionals (2.13) as

$$\bar{I} [\partial_z^b [g - \tilde{g}]] \equiv J_{10} \left[(\partial_z^b g_\kappa(z))_{\kappa \gg 1} - \partial_z^b \tilde{g}_\kappa(z) \right] + I_{10} \left[\overline{\partial_z^b g_\kappa(z)} \right] - I_{10} [\partial_z^b \tilde{g}_\kappa(z)], \quad (5.6)$$

and computed numerically as

$$\underline{I} [\partial_z^b [g - \tilde{g}]] \equiv J_{25} \left[(\partial_z^b g_\kappa(z))_{\kappa \gg 1} - \partial_z^b \tilde{g}_\kappa(z) \right] + I_{25} \left[\underline{\partial_z^b g_\kappa(z)} \right] - I_{25} [\partial_z^b \tilde{g}_\kappa(z)]. \quad (5.7)$$

Because of the defined behavior of the piecewise approximations (5.4) and (5.5) in the large κ region, \bar{I} is insensitive to the choice of the cutoff parameter, as long as $\bar{\Lambda} > \kappa_{R_0}, \kappa_{R_2}$. Therefore, we arbitrarily take $\bar{\Lambda} = 10$.

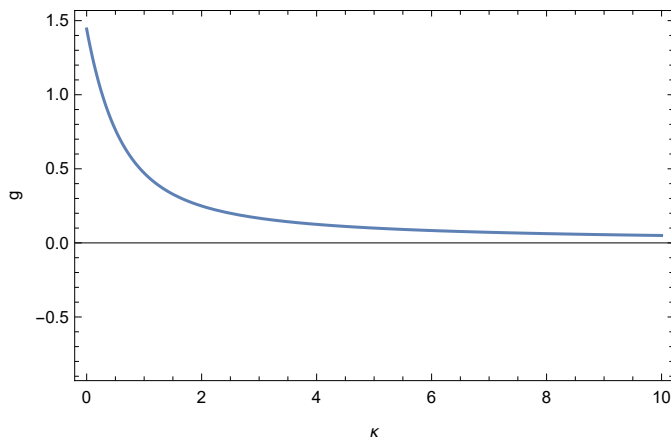


FIG. 3. The numerical Green function $\underline{g}_\kappa(z)$ for $V(z) = z^6$ and $z = 0.01$.

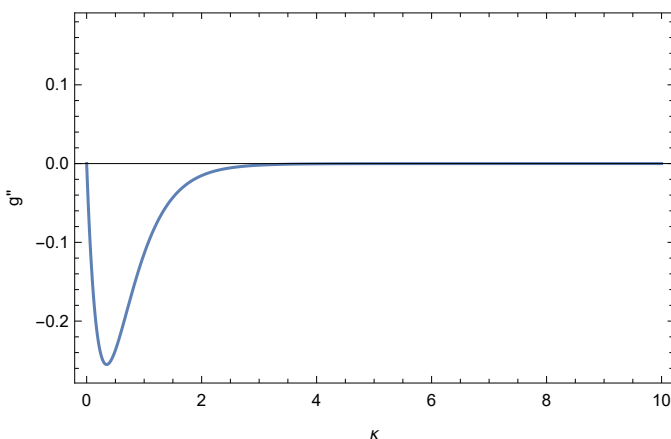


FIG. 4. The second derivative of the numerical Green function $\underline{\partial_z^2 g}_\kappa(z)$ for $V(z) = z^6$ and $z = 0.01$.

The numerical cutoff parameter $\underline{\Lambda} = 25$ reflects the region where the numerical solution is valid. For values slightly larger than $\kappa = 25$, the second derivative of the computed Green function starts decreasing. Although minuscule, this behavior is undesirable and disagrees with the expected qualitative behavior of $\partial_z^2 g_\kappa(z)$.

VI. THE ENERGY DENSITY INSIDE THE SEXTIC WALL

Using the scheme developed in the last section and [13, Eq. (5.11)], we approximate the renormalized energy density inside the sextic wall $V(z) = z^6$. The arbitrary mass scale μ is taken to be 1.

Following the notation introduced in [12], we define $\beta \equiv \xi - \frac{1}{4}$, where ξ is the conformal parameter. Plugging the sextic potential into [13, Eq. (5.11)] yields

$$\langle T^{00} \rangle_R = \langle T^{00} \rangle [I[g - \tilde{g}]] + \frac{96\beta - z^8(528\beta + z^8 + 32)}{128\pi^2 z^4} + \frac{3z^4(-120\beta + z^8 - 10) \ln z}{32\pi^2}, \quad (6.1)$$

where the first term is given by [13, Eq. (6.3)] as

$$\langle T^{00} \rangle [I[g - \tilde{g}]] = - \left(I \left[\frac{\kappa^2}{3} [g - \tilde{g}] \right] + I [\beta \partial_z^2 [g - \tilde{g}]] \right). \quad (6.2)$$

We compute this term using the analytical and numerical functionals \bar{I} and \underline{I} defined in Eqs. (5.6) and (5.7), respectively. The corresponding integrals were evaluated numerically for 20 evenly-spaced values of z and interpolated.

Figs. 5 and 6 show the energy density for various conformal parameters in the small and large z regimes. The corresponding relative errors are shown in Fig. 7.

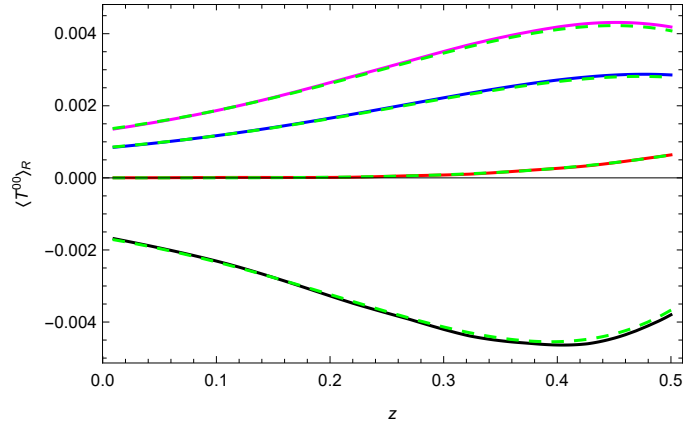


FIG. 5. The approximated energy density inside the sextic wall for $\beta = 1/20$, $\beta = 0$, $\beta = -1/12$ (the conformal value), and $\beta = -1/4$ (the minimal coupling value), from top to bottom. The dashed green curves are the corresponding numerical energy densities.

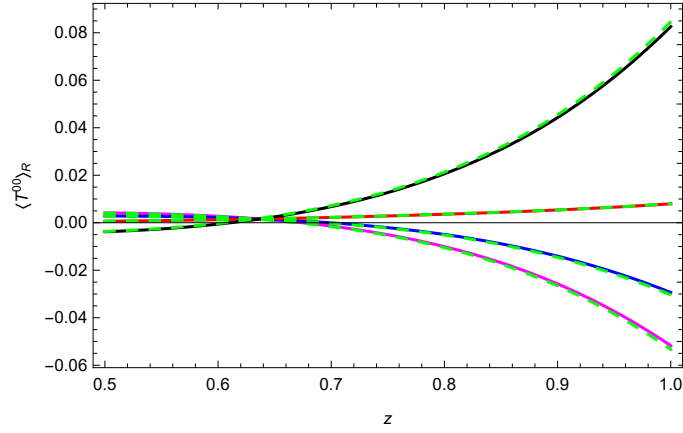


FIG. 6. The energy density inside the sextic wall for large z . The energy density clearly changes signs in the large z region.

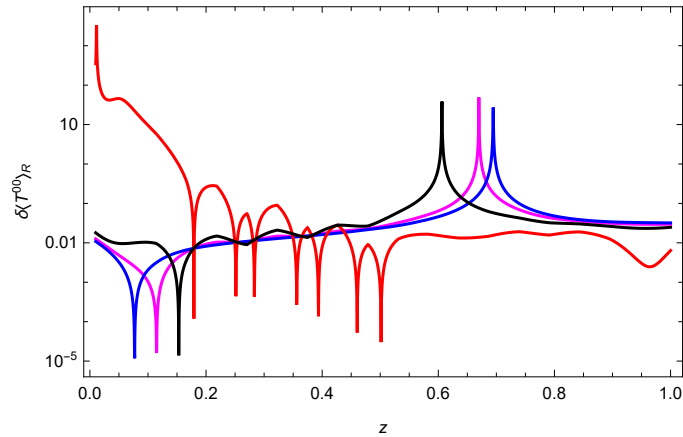


FIG. 7. The relative errors in the approximated energy density inside the sextic wall. The curves show $\beta = 1/20$ in magenta, $\beta = 0$ in blue, $\beta = -1/12$ (the conformal value) in red, and $\beta = -1/4$ (the minimal coupling value) in black. The peaks occur where the numerical energy densities vanish; the absolute error is small there.

VII. THE PRESSURE INSIDE THE SEXTIC WALL

Similarly to the energy density, plugging the sextic wall $V(z) = z^6$ and the arbitrary mass scale $\mu = 1$ into [13, Eq. (5.11)] yields

$$\langle T^{zz} \rangle_R = \langle T^{zz} \rangle [I [g - \tilde{g}]] + \frac{z^{16} + 12z^8 - 24}{128\pi^2 z^4} - \frac{3z^{12} \ln z}{32\pi^2}, \quad (7.1)$$

where the first term is given by [13, Eq. (2.13d)] as

$$\langle T^{zz} \rangle [I [g - \tilde{g}]] = I \left[\frac{1}{4} \partial_z^2 [g - \tilde{g}] \right] - I [(\kappa^2 + z^6) [g - \tilde{g}]], \quad (7.2)$$

and is again computed using \bar{I} and \underline{I} .

As evident in Figs. 8 and 9, the approximated pressure is inaccurate in the small z regime, despite being numerically small. Had the range of Fig. 8 been restricted to that of Fig. 5, the curves would seem drastically different. In this region, the pressure is significantly smaller than the typical error in the approximations (5.4) and (5.5), rendering its accurate computation unfeasible.

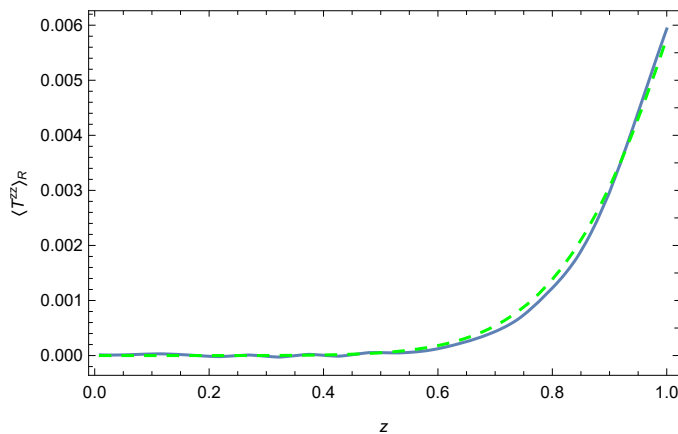


FIG. 8. The approximated pressure (in light blue) and its numerical counterpart (in green dashes) inside the sextic wall.

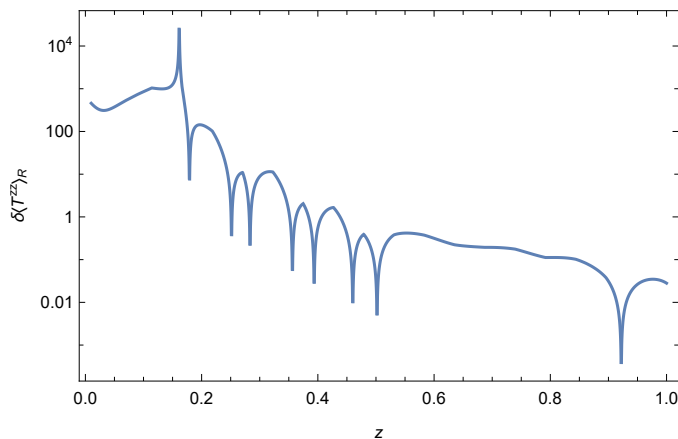


FIG. 9. The relative error in the approximated pressure inside the sextic wall.

VIII. CONSERVATION LAWS

Since the trace identity and conservation law associated with $\langle T^{\mu\nu} \rangle_R$ depend on the vacuum expectation value of ϕ^2 , its renormalization must be consistent with the renormalization of the stress tensor [13, Eq. (5.11)]. We adapt

the general prescription given in [14] to the model (2.2). This Lagrangian density was obtained from [14, Eq. (5)] by taking $\lambda = 1$. Following our convention, we also fix the arbitrary mass scale $\mu = 1$. With the $C_j = 0$, the renormalized field squared is given above [14, Eq. (36)] as

$$\langle \phi^2 \rangle_R = \frac{1}{16\pi^2} (V \ln V - V + O(V^{-1})).$$

As discussed in [14, p. 10], this renormalization process is not unique. Addition of ΥV , for any constant Υ , results in a conserved stress tensor. Therefore, we take $\Upsilon = 1$ to cancel the term proportional to V . Comparing this to [13, Eq. (5.2)] (with $\delta = 0$), we identify the $O(V^{-1})$ term with $I [g_\kappa(z) - g_\kappa^{(0)}(z)]$, where

$$g_\kappa^{(0)}(z) = \frac{1}{2\sqrt{\kappa^2 + V(z)}}$$

is the zeroth-order WKB approximation of $g_\kappa(z)$ [13, Appendix A]. We obtain the renormalization

$$\langle \phi^2 \rangle_R = I [g_\kappa(z) - g_\kappa^{(0)}(z)] + \frac{V \ln V}{16\pi^2}. \quad (8.1)$$

For the sextic wall $V(z) = z^6$, we obtain

$$\langle \phi^2 \rangle_R \equiv I_R [g_\kappa(z)] = I \left[g_\kappa(z) - \frac{1}{2\sqrt{\kappa^2 + z^6}} \right] + \frac{3z^6 \ln z}{8\pi^2}. \quad (8.2)$$

This allows us to renormalize the trace identity and the conservation law. The trace identity [13, Eq. (5.10)] is renormalized as

$$\langle T^\mu{}_\mu \rangle_R + V I_R - 3 \left(\xi - \frac{1}{6} \right) \partial_z^2 I_R = \frac{1}{32\pi^2} \left(V^2 - \frac{1}{3} V'' \right). \quad (8.3)$$

The consistency of our results with this identity is demonstrated in Fig. 10.

Since $\langle T^{xx} \rangle_R = \langle T^{yy} \rangle_R = -\langle T^{00} \rangle_R$, the divergence $\partial_\mu \langle T^{\mu\nu} \rangle_R$ simplifies to $\partial_z \langle T^{zz} \rangle_R$. Therefore, the renormalized conservation law

$$\partial_\mu \langle T^{\mu\nu} \rangle_R + \frac{1}{2} \partial^\nu V \langle \phi^2 \rangle_R = 0,$$

simplifies to

$$\partial_z \langle T^{zz} \rangle_R = -\frac{V'}{2} I_R. \quad (8.4)$$

Fig. 11 shows both sides of the renormalized conservation law.

IX. REPRODUCING THE ENERGY DENSITY FOR THE QUADRATIC WALL

To further verify the approximations (5.4) and (5.5), we reproduce the energy density for the quadratic wall, which was computed from the exact Green function in [13]. As in the sextic wall, we choose the endpoints to be in the domain of validity of the perturbative and WKB expansions. These were taken to be $\kappa_{L_0} = 1$ and $\kappa_{R_0} = 6$ for the Green function, and $\kappa_{L_2} = 1$ and $\kappa_{R_2} = 8$ for its second derivative. We calculate the energy density using Eqs. (6.1) and (6.2), as before.

For comparison purposes, the data associated with [13, Fig. 4] was obtained from the authors. Figs. 12 and 13 clearly demonstrate the consistency of our approximation with the calculation conducted in [13]. Certain technical problems in the numerical work in [13] (for reasons completely unrelated to any uncertainty in the present work) needed to be resolved by an *ad hoc* fitting of one constant [13, Eq. (7.12)]. Therefore, the observed consistency serves as a welcome confirmation of that calculation as well as ours.

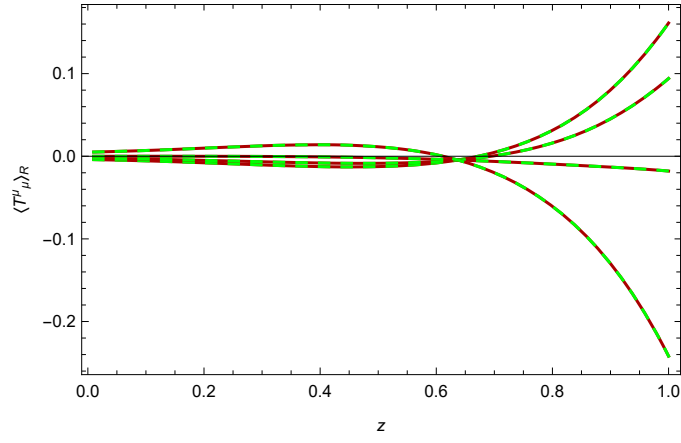


FIG. 10. The approximated trace (in dark red) and the trace identity (8.3) with $I_R \mapsto \bar{I}_R$ (in green dashes) inside the sextic wall. The curves show $\beta = 1/20, 0, -1/12, -1/4$, from top-right to bottom-right.

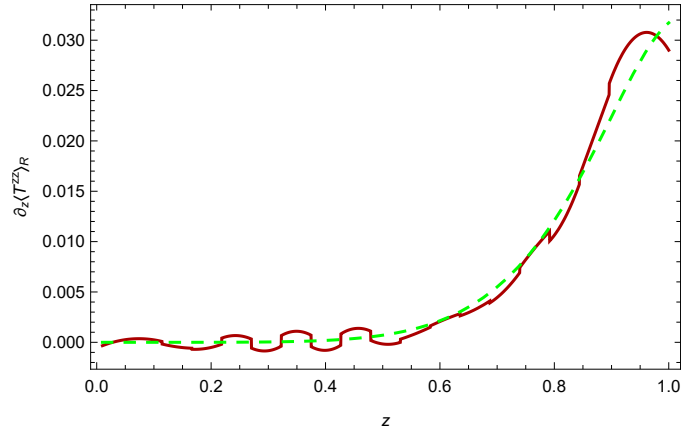


FIG. 11. The approximated divergence (in dark red) and $-\bar{I}_R V'/2$ of Eq. (8.4) (in green dashes) inside the sextic wall. The apparent “wiggles” are an artifact of the spline approximation.

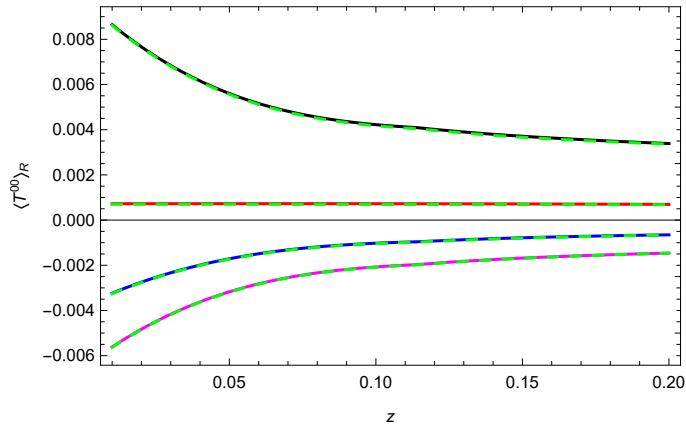


FIG. 12. The approximated energy density for $\alpha = 2$ obtained from \bar{I} for $\beta = 1/20, 0, -1/12, -1/4$, from bottom to top (in solid curves). The dashed green curves are the corresponding energy densities from the data of [13, Fig. 4].

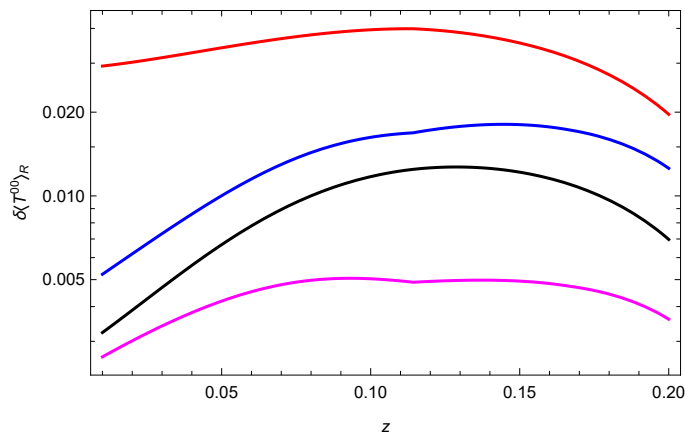


FIG. 13. The relative errors in the approximated energy density inside the quadratic wall. The curves show $\beta = 1/20, -1/4, 0, -1/12$, from bottom to top (the colors are the same as in Fig. 12).

X. CONCLUSION

The methodologies developed in this paper successfully generalize the analysis and results given in [13] to arbitrarily “hard” power walls. Using high order perturbative and WKB expansions, we approximated the Green function and its relevant derivatives to high accuracy in the small and large κ regimes.

These approximations were used to interpolate the functions in the intermediate regime. By constructing a spline that matches the perturbative and WKB expansions at appropriate endpoints, we obtained piecewise analytical approximations of the Green function and its second derivative. These approximations were then used to compute the renormalized stress tensor inside the sextic wall.

To validate the approximated results, we compared them to their numerical counterparts. The numerical approximations were obtained by discretizing the equation of motion of the scalar field ϕ and solving the resulting matrix equation. The solution process was optimized by utilizing techniques of numerical linear algebra and parallel computing. The approximated energy density, and to a reasonable extent the pressure, agree with their numerical counterparts, indicating their validity. The approximated stress tensor also satisfies the renormalized trace identity and conservation law.

To further verify the validity of the developed approximation scheme, we reproduced the energy density for the quadratic wall, which was computed exactly in [13]. Our results agree with [13, Fig. 4] within reasonable error.

The analytical and numerical methods are complementary. They tend to fail or become problematical in different regimes. Furthermore, both approaches require *ad hoc* elements, and their agreement reassures the obtained results. The adaptivity of the analytical approach to arbitrary orders of accuracy and the insight it grants into the qualitative behavior of the Green function are advantages over the numerical calculations.

In future work, we hope to generalize and improve the approximation method in the intermediate κ regime. The current method relies on fixing arbitrary endpoints for the construction of the spline which is neither optimal nor valid for all values of z . A better method to select the endpoints may make use of the remainders associated with the perturbation and WKB series, which are yet to be calculated.

ACKNOWLEDGMENTS

This research was supported by undergraduate research funds from the Texas A&M University Department of Physics and Astronomy. The numerical portion of the work relied on the advanced computing resources provided by Texas A&M High Performance Research Computing.

Vivek Sarin, who served as co-advisor on [15], provided guidance about the numerical solution scheme. Kimball Milton gave constructive feedback and provided the data from [13] used in Figs. 12 and 13.

David Lujan participated in some of the earliest work on this project, and Timothy Bates is participating in the most recent parts and has provided valuable comments on the manuscript. Helpful remarks were made by Colin Whisler, Pushpa Kalauni, Gerard Kennedy, Justin Wilson, and Nima Pourtolami.

Appendix A: THE NUMERICAL SOLUTION

1. Discretization

In Secs. VII and VI, we use the numerical counterpart of \bar{I} , namely \underline{I} , to generate numerical approximations of the energy density and pressure. As the analogue of the operator (5.6), it is composed of the numerical Green function, which is related to the numerical basis solutions $\underline{F}_\kappa(z)$ and $\underline{G}_\kappa(z)$ via Eq. (2.6). To obtain them, we convert the differential equation (2.7) to a matrix equation. This discretization takes the boundary conditions (2.8) into account, which results in the nonsingularity of the matrix. The discretized equation may be solved by consecutive Gaussian eliminations for all desired values of κ . In each iteration, κ is treated as a constant parameter. For numerical stability we used a Cholesky factorization. Details are provided in [15].

We discretize the entities composing Eq. (2.7) as

$$\vec{z} = \begin{bmatrix} z_0 \\ z_1 \\ \vdots \\ \vdots \\ z_{m+1} \end{bmatrix}, \quad \vec{V} = \begin{bmatrix} V(z_0) \\ V(z_1) \\ \vdots \\ \vdots \\ V(z_{m+1}) \end{bmatrix}, \quad \vec{y} = \begin{bmatrix} y_0 \\ y_1 \\ \vdots \\ \vdots \\ y_{m+1} \end{bmatrix}, \quad (\text{A1})$$

where $V(z)$ is the soft wall (2.1). We denote the uniform interval width by $h \equiv z_{i+1} - z_i$.

Since the values y_0 and y_{m+1} are known at the boundary points z_0, z_{m+1} , we solve Eq. (2.7) in the domain $[z_1, \dots, z_m]$. With this goal in mind, we seek a discretization of the differential operator acting on the left hand side of Eq. (2.7) which yields m equations for the m unknowns $\{y_1, \dots, y_m\}$. The second derivative is approximated by the sixth-order centered finite difference formula [19, 20]

$$180h^2 \partial_z^2 y|_{z_i} \approx 2y_{i-3} - 27y_{i-2} + 270y_{i-1} - 490y_i + 270y_{i+1} - 27y_{i+2} + 2y_{i+3}, \quad (\text{A2})$$

for $2 < i < m - 1$. Near the boundary, we use the formulae [19, 20]

$$\begin{aligned} 180h^2 \partial_z^2 y|_{z_1} &\approx 126y_0 - 70y_1 - 486y_2 + 855y_3 - 670y_4 + 324y_5 - 90y_6 + 11y_7, \\ 180h^2 \partial_z^2 y|_{z_2} &\approx -11y_0 + 214y_1 - 378y_2 + 130y_3 + 85y_4 - 54y_5 + 16y_6 - 2y_7, \\ 180h^2 \partial_z^2 y|_{z_{m-1}} &\approx -2y_{m-6} + 16y_{m-5} - 54y_{m-4} + 85y_{m-3} + 130y_{m-2} - 378y_{m-1} + 214y_m - 11y_{m+1}, \\ 180h^2 \partial_z^2 y|_{z_m} &\approx 11y_{m-6} - 90y_{m-5} + 324y_{m-4} - 670y_{m-3} + 855y_{m-2} - 486y_{m-1} - 70y_m + 126y_{m+1}. \end{aligned} \quad (\text{A3})$$

The portion of the formulae independent of the boundary conditions y_0 and y_{m+1} can be combined into an $m \times m$ matrix. This matrix will operate on the column vector $[y_1, \dots, y_m]^T$ to produce $\partial_z^2 y$ inside the interval.

The boundary terms can be added to the appropriate elements after the multiplication. According to the formulae (A2) and (A3), the boundary terms appear in the approximations for $y''(z_1)$, $y''(z_2)$, $y''(z_3)$, $y''(z_{m-2})$, $y''(z_{m-1})$, and $y''(z_m)$. We then approximate $\partial_z^2 y$ inside the interval as

$$\begin{bmatrix} y''(z_1) \\ y''(z_2) \\ y''(z_3) \\ y''(z_4) \\ y''(z_5) \\ \vdots \\ y''(z_{m-4}) \\ y''(z_{m-3}) \\ y''(z_{m-2}) \\ y''(z_{m-1}) \\ y''(z_m) \end{bmatrix} \approx \frac{1}{180h^2} \underbrace{\begin{bmatrix} -70 & -486 & 855 & -670 & 324 & -90 & 11 & 0 & \cdots & 0 \\ 214 & -378 & 130 & 85 & -54 & 16 & -2 & 0 & \cdots & 0 \\ -27 & 270 & -490 & 270 & -27 & 2 & 0 & 0 & \cdots & 0 \\ 2 & -27 & 270 & -490 & 270 & -27 & 2 & 0 & \cdots & 0 \\ 0 & 2 & -27 & 270 & -490 & 270 & -27 & 2 & \cdots & \vdots \\ \vdots & \vdots & \ddots & \ddots & \ddots & \ddots & \ddots & \ddots & \ddots & \vdots \\ \vdots & \vdots & & \ddots & \ddots & \ddots & \ddots & \ddots & \ddots & 2 \\ 0 & \cdots & 0 & 0 & 2 & -27 & 270 & -490 & 270 & -27 \\ 0 & \cdots & 0 & -2 & 16 & -54 & 85 & 130 & -378 & 214 \\ 0 & \cdots & 0 & 11 & -90 & 324 & -670 & 855 & -486 & -70 \end{bmatrix}}_{D_z^2} \begin{bmatrix} y_1 \\ y_2 \\ y_3 \\ y_4 \\ y_5 \\ \vdots \\ y_{m-4} \\ y_{m-3} \\ y_{m-2} \\ y_{m-1} \\ y_m \end{bmatrix} + \frac{1}{180h^2} \underbrace{\begin{bmatrix} 126y_0 \\ -11y_0 \\ 2y_0 \\ 0 \\ 0 \\ \vdots \\ 0 \\ 0 \\ 2y_{m+1} \\ -11y_{m+1} \\ 126y_{m+1} \end{bmatrix}}_{\vec{b}}. \quad (\text{A4})$$

Finally, using the discretization (A4), we convert Eq. (2.7) into the matrix equation

$$\left(-D_z^2 + \text{diag}(\vec{V}) + \kappa^2 \mathbb{1}\right) \begin{bmatrix} y_1 \\ \vdots \\ y_m \end{bmatrix} = \vec{b}. \quad (\text{A5})$$

2. Boundary Conditions

To solve for $F_\kappa(z)$, we approximate the decaying behavior by taking a sufficiently large value of z_{m+1} and demanding that $F_\kappa(z_{m+1})$ effectively vanishes. Using Eq. (4.2), we conclude that $z_{m+1} = 10$ can be taken to be the interval endpoint for our purposes.

Since both conditions for $G_\kappa(z)$ in Eq. (2.8) are given at $z = 0$, we cannot solve for it using Eq. (A5) directly. However, we can solve a related boundary value problem, obtain the solution $\tilde{G}_\kappa(z)$, and deduce $G_\kappa(z)$ from it. Since $G_\kappa(z)$ is defined to be exponentially increasing, we enforce the boundary condition $\tilde{G}_\kappa(0) = G_\kappa(0) = 0$, and guess a larger boundary condition for $\tilde{G}_\kappa(z)$ at a reasonable endpoint z_{m+1} , as shown in Table A1. The function $\tilde{G}_\kappa(z)/\tilde{G}'_\kappa(0)$ clearly satisfies the initial conditions (2.8) and must coincide with $G_\kappa(z)$ from uniqueness arguments.

TABLE A1. Summary of the boundary conditions used to solve Eq. (A5).

Function	z_0	y_0	z_{m+1}	y_{m+1}
$F_\kappa(z)$	0	1	10	0
$\tilde{G}_\kappa(z)$	0	0	2	1

Appendix B: PRELIMINARY METHODOLOGIES

The central problem of this paper is bridging the gap between perturbative and WKB approximations. In the exterior of the soft wall, such an operation was needed only once: for the function called $\gamma_-(\kappa)$ in [12, Sec. IV and Figs. 6–7]. A simple spline between low-order expansions was remarkably successful there. In retrospect, this was a stroke of luck; in the interior calculation, bridging was needed more often, and the elementary methodology was much less successful. Solving this problem took five years and the participation of three “generations” of undergraduate research assistants. One lesson is that no method is guaranteed to be a permanent solution, and sometimes it pays to return to methods previously abandoned. Therefore, a brief account of some false starts may be of value.

In our initial approach, we attempted to construct piecewise solutions for the various relevant functions, such as $F_\kappa(z)$, $G_\kappa(z)$, and $c_F(\kappa)$ (the link between the WKB approximation of $F_\kappa(z)$ and the initial data (2.8); see [12, (3.9a)]).

Initially we developed the small- κ and large- κ expansions only to rather low order, with a minimum of computer assistance. In particular, we implemented (3.1) only for $n = 1$, because *Mathematica* cannot evaluate the integrals for $n = 2$. We picked various simple spline forms to approximate the functions between these two regimes, and fit the parameters to best agree with both expansions. The partition of the κ domain into the three regimes is described in Table A2. The various spline forms tested are shown in Table A3. It rapidly became clear that no single spline form could give acceptable results in all cases.

TABLE A2. The piecewise partition of the κ domain used to construct the spline.

Function	Description	Approximation type
$l(\kappa)$	the “left” expression	perturbation expansion
$r(\kappa)$	the “right” expression	WKB expansion
$m(\kappa)$	the “middle” expression	2-parameter spline

Given a form of $m(\kappa)$, we searched for endpoints κ_L and κ_R which would mark the transitions between the functions in Table A2. The conditions imposed on the spline demanded that m matched l and r at κ_L and κ_R , respectively, to first order. This amounted to finding a zero of the vector-valued function

$$\vec{g}(\vec{x}) = \begin{pmatrix} l'(x_1) - m'(x_1) \\ r'(x_2) - m'(x_2) \end{pmatrix}.$$

TABLE A3. The various spline forms tested.

Spline form	Formula
linear	$m(\kappa) = A\kappa + B$
quadratic	$m(\kappa) = A\kappa^2 + B$
reciprocal	$m(\kappa) = (A\kappa + B)^{-1}$
exponential	$m(\kappa) = \exp(A\kappa + B)$

The parameters A and B were implicitly functions of x_1 and x_2 as well, as the spline function m needed to satisfy the conditions. Thus generically, both components of \vec{g} were functions of both x_1 and x_2 .

We then used a multidimensional version of Newton's method to iteratively find the zero of the function. Using the Jacobian matrix, $J_{ij} = \frac{\partial g_i}{\partial x_j}$, each iteration of the algorithm computed

$$\vec{x}_{n+1} = \vec{x}_n - J^{-1} \cdot \vec{g}(\vec{x}_n).$$

If the algorithm converged, the resulting values of κ_L , κ_R , A , and B would give a spline approximation to the solution in the intermediate regime.

Unfortunately, even when a suitable spline was found and the Newton iteration converged, the accuracy of the results often was disappointing. We made some strategic changes: first, to interpolate the Green function g_κ directly, instead of its ingredients F_κ and G_κ , and second, to replace the spline by a Padé approximant. The 2-point $[\ell/m]$ Padé approximant of a function $f(\kappa)$, as described in [21], is the rational function $P_\ell(\kappa)/Q_m(\kappa)$ whose power series matches $f(\kappa)$ as much as possible at two given points. As shown in [21, Sec. IV], the matching requirements yield linear constraints on the coefficients of $P_\ell(\kappa)$ and $Q_m(\kappa)$. These equations are solved to determine the approximant $P_\ell(\kappa)/Q_m(\kappa)$.

We constructed the 2-point $[4/4]$ Padé approximant of $g_\kappa(z)$ at $\kappa = 0$ and ∞ , matching to the coefficients of the first four terms in (3.3) and the first five in the expansion of the dominant term in (4.3) as a series in $1/\kappa$. The resulting approximant was differentiated twice with respect to z to approximate $\partial_z^2 g_\kappa(z)$.

Initial results of the Padé method were encouraging, but again not sufficiently accurate for our purposes. When the order was increased, spurious poles appeared in the approximant. (This is a well known disease of the Padé method.) A pole can be bypassed by constructing a spline across it, but this extra *ad hoc* step has no strong advantage over a pure spline.

Meanwhile, numerical calculations were being carried out for comparison with all these analytical approximations. The basis functions $F_\kappa(z)$ and $G_\kappa(z)$ were computed by the NDSOLVE routine in *Mathematica*, as well as the Numerical Calculus package (to compute the solution's derivatives). The initial conditions for $F_\kappa(z)$ were obtained from its first-order Fröman approximation [13, Appendix A] at $z = 10$. While this process often yielded a solution, it was unstable and failed unexpectedly for some values of z .

For both the numerical and the analytical solutions, therefore, we abandoned our original preference for low-tech methods. The expansions (3.3) and (4.3) have been implemented to quite high orders and successfully bridged by splines, as reported in Sec. V. The numerical work has been moved from *Mathematica* to professional numerical-analysis software as reported in Sec. V and Appendix A.

-
- [1] H. B. G. Casimir, On the attraction between two perfectly conducting plates, *Proc. Kon. Ned. Akad. Wet.* **51**, 793 (1948).
 - [2] M. Fierz, Zur anziehung leitender ebener im vakuum, *Helv. Phys. Acta* **33**, 855 (1960).
 - [3] T. H. Boyer, Quantum zero-point energy and long-range forces, *Ann. Phys.* **56**, 474 (1970).
 - [4] C. M. Bender and P. Hays, Zero-point energy of fields in a finite volume, *Phys. Rev. D* **14**, 2622–2632 (1976).
 - [5] R. Estrada, S. A. Fulling, and F. D. Mera, Surface vacuum energy in cutoff models: pressure anomaly and distributional gravitational limit, *Journal of Physics A: Mathematical and Theoretical* **45**, 455402 (2012).
 - [6] I. Griniasty and U. Leonhardt, Casimir stress inside planar materials, *Phys. Rev. A* **96**, 032123 (2017).
 - [7] I. Griniasty and U. Leonhardt, Casimir stress in materials: Hard divergency at soft walls, *Phys. Rev. B* **96**, 205418 (2017).
 - [8] P. Parashar, K. A. Milton, Y. Li, H. Day, X. Guo, S. A. Fulling, and I. Cavero-Peláez, Quantum electromagnetic stress tensor in an inhomogeneous medium, *Phys. Rev. D* **97**, 125009 (2018).
 - [9] Y. Li, K. A. Milton, X. Guo, G. Kennedy, and S. A. Fulling, Casimir forces in inhomogeneous media: Renormalization and the principle of virtual work, *Phys. Rev. D* **99**, 125004 (2019).
 - [10] J. Bouas, S. Fulling, F. Mera, K. Thapa, C. Trendafilova, and J. Wagner, Investigating the spectral geometry of a soft wall, in *Proc. Symp. Pure Math*, 84, edited by A. H. B. et al (2012) pp. 139–154.
 - [11] K. A. Milton, Hard and soft walls, *Physical Review D* **84**, 065028 (2011).

- [12] S. Murray, C. Whisler, S. Fulling, J. Wagner, H. Carter, D. Lujan, F. Mera, and T. Settlemyre, Vacuum energy density and pressure near a soft wall, *Physical Review D* **93**, 105010 (2016).
- [13] K. A. Milton, S. A. Fulling, P. Parashar, P. Kalauni, and T. Murphy, Stress tensor for a scalar field in a spatially varying background potential: Divergences, “renormalization”, anomalies, and Casimir forces, *Physical Review D* **93**, 085017 (2016).
- [14] S. A. Fulling, T. E. Settlemyre, and K. A. Milton, Renormalization for a scalar field in an external scalar potential, *Symmetry* **10**, 54 (2018).
- [15] A. Shayit, *Vacuum Energy in General Power Wall Models*, Undergraduate Research Scholars Program, Texas A&M University (2021), available electronically from <https://hdl.handle.net/1969.1/194332>.
- [16] M. Faierman, Generalized parabolic cylinder functions, *Asymptotic Analysis* **5**, 517 (1992).
- [17] J. Campbell, Computation of a class of functions useful in the phase-integral approximation. I. Results, *Journal of Computational Physics* **10**, 308 (1972).
- [18] J. Gustavus, Calculation of even order N 's used in the Fröman phase-integral approximation, Math. 401 class paper, Texas A&M University (1991).
- [19] C. Taylor, Finite difference coefficients calculator, <https://web.media.mit.edu/~crtaylor/calculator.html> (2019).
- [20] B. Fornberg, Generation of finite difference formulas on arbitrarily spaced grids, *Mathematics of Computation* **51**, 699 (1988).
- [21] J. Čížek, E. J. Weniger, P. Bracken, and V. Špirko, Effective characteristic polynomials and two-point Padé approximants as summation techniques for the strongly divergent perturbation expansions of the ground state energies of anharmonic oscillators, *Physical Review E* **53**, 2925 (1996).
- [22] G. H. Golub and C. F. Van Loan, *Matrix Computations*, 4th ed., Johns Hopkins studies in the mathematical sciences (The Johns Hopkins University Press, Baltimore, 2013).
- [23] *Terra User's Guide*, Texas A&M High Performance Research Computing (2018).